ARTICLE   OPEN

Cryo-EM reveals ligand induced allostery underlying InsP$_3$R channel gating

Guizhen Fan[1], Mariah R. Baker[1], Zhao Wang[2], Alexander B. Seryshev[1], Steven J. Ludtke[2], Matthew L. Baker[2] and Irina I. Serysheva[1]

Inositol-1,4,5-trisphosphate receptors (InsP$_3$Rs) are cation channels that mobilize Ca^{2+} from intracellular stores in response to a wide range of cellular stimuli. The paradigm of InsP$_3$R activation is the coupled interplay between binding of InsP$_3$ and Ca^{2+} that switches the ion conduction pathway between closed and open states to enable the passage of Ca^{2+} through the channel. However, the molecular mechanism of how the receptor senses and decodes ligand-binding signals into gating motion remains unknown. Here, we present the electron cryo-microscopy structure of InsP$_3$R1 from rat cerebellum determined to 4.1 Å resolution in the presence of activating concentrations of Ca^{2+} and adenophostin A (AdA), a structural mimetic of InsP$_3$ and the most potent known agonist of the channel. Comparison with the 3.9 Å-resolution structure of InsP$_3$R1 in the Apo-state, also reported herein, reveals the binding arrangement of AdA in the tetrameric channel assembly and striking ligand-induced conformational rearrangements within cytoplasmic domains coupled to the dilation of a hydrophobic constriction at the gate. Together, our results provide critical insights into the mechanistic principles by which ligand-binding allosterically gates InsP$_3$R channel.

INTRODUCTION

Inositol 1,4,5-trisphosphate receptors (InsP$_3$Rs) constitute a functionally important class of intracellular Ca^{2+} channels that are capable of converting a wide variety of cellular signals (e.g., hormones, neurotransmitters, growth factors, light, odorants, signaling proteins) to intracellular calcium signals, which trigger markedly different cellular actions ranging from gene transcription to secretion, from proliferation to cell death.[1–4] The cellular signals are transmitted to the receptor by the secondary messenger molecule inositol 1,4,5-trisphosphate (InsP$_3$), the primary agonist of InsP$_3$Rs, generated within an essential intracellular signaling pathway initiated by phospholipase C. There is a general consensus that activation of channel gating is associated with conformational rearrangements at the inner pore-lining helix bundle that are triggered by InsP$_3$ binding within the first 600 residues of the InsP$_3$R protein.[5,6] This functional coupling has been experimentally demonstrated through electrophysiological, ligand-binding and mutagenesis studies,[1,7] however the precise molecular mechanism by which InsP$_3$ exerts its effect on InsP$_3$R function is still largely unknown. Our previous study described the 4.7 Å resolution electron cryomicroscopy (cryo-EM) structure of the full-length tetrameric InsP$_3$R1 channel in a ligand-free (Apo-state), which revealed a network of intra- and inter-domain interfaces that might be responsible for the conformational coupling between ligand-binding and gating activation.[5] To further investigate how the structure of the InsP$_3$R channel allows for ligand-initiated gating, we have now determined the 3D structure of InsP$_3$R1 bound to adenophostin A (AdA), a highly potent agonist of InsP$_3$Rs,[8,9] to 4.1 Å resolution using single-particle cryo-EM analysis. In this study, we have also extended our structural analysis of InsP$_3$R1 in an Apo-state to 3.9 Å resolution. Together, these structures reveal how InsP$_3$R1 channel performs its mechanical work through ligand-driven allostery that removes the molecular barrier within the ion permeation pathway and allows for Ca^{2+} translocation across the membrane.

RESULTS

Structure of AdA-InsP$_3$R1

To understand how ligand-binding triggers a drastic change in the permeability of InsP$_3$R channel to specific ions, we determined the structure of InsP$_3$R1 in the presence of activating concentrations of AdA (100 nM) and Ca^{2+} (300 nM), which works as a co-agonist to promote channel opening, as demonstrated in numerous electrophysiological studies.[9–13]

From a structural perspective, AdA is intriguing because this fungal glyconucleotide metabolite mimics InsP$_3$ by acting as a full agonist that binds to InsP$_3$R1 with ~10-times greater affinity and ~12-times more potency in opening the channel than InsP$_3$.[9,10,14] Previous studies suggest that the 3″,4″-bisphosphate and 2″-hydroxyl groups of AdA mimic the essential 4,5-bisphosphate and 6-hydroxyl of InsP$_3$, respectively (Supplementary information, Fig. S1a).[8,10,15] The 2′-phosphate is believed, at least in part, to mimic the 1-phosphate of InsP$_3$.[8,16,17] This structural similarity between the two ligands likely accounts for the competitive binding of AdA to the same InsP$_3$-binding domains (Supplementary information, Fig. S1b, c). However, the molecular basis for the unique properties of AdA is unknown, as is the mechanism of channel opening upon ligand binding.

[1]Department of Biochemistry and Molecular Biology, Structural Biology Imaging Center, McGovern Medical School at The University of Texas Health Science Center at Houston, 6431 Fannin Street, Houston, TX 77030, USA and [2]Verna and Marrs McLean Department of Biochemistry and Molecular Biology, CryoEM and CryoET Core, Baylor College of Medicine, One Baylor Plaza, Houston, TX 77030, USA
Correspondence: Irina I. Serysheva (irina.i.serysheva@uth.tmc.edu)
These authors contributed equally: Guizhen Fan and Mariah R. Baker

Cryo-EM structure of ligand-bound IP3R1 channel
G. Fan et al.

1159

In this study we collected large data sets of both AdA-InsP$_3$R1 and Apo-InsP$_3$R1. Due to the potential for partial ligand occupancy, the AdA-InsP$_3$R1 map was generated using standard single-particle 3D reconstruction techniques combined with a masked focused classification approach to achieve consistency among the particles used in the reconstruction (Supplementary information, Figs. S2, S3, Table S1; see Methods). The final maps were of sufficient resolution to enable an unambiguous interpretation of the protein structure (Supplementary information, Figs. S2, S4). Map resolvability in both states permitted a backbone trace for ~80% of the entire protein, as well as a full atomistic representation in specific domains (~37.5% of the entire protein) (Supplementary information, Fig. S5).

The map resulting from the class of AdA-bound InsP$_3$R1 particles exhibited robust density bridging the β-TF2 and ARM1 domains (Fig. 1). The location of this density is consistent with the location of the bound InsP$_3$ molecule in the crystal structures of isolated ligand-binding domains (LBDs) (Supplementary information, Fig. S6a, c).[18,19] Therefore, the densities identified at the β-TF2/ARM1 clefts in the AdA-InsP$_3$R1 map were assigned to the bound AdA molecule.

The 3D structure of AdA-InsP$_3$R1 matches an overall arrangement of the Apo-InsP$_3$R, also determined to 3.9 Å resolution in the present study (Supplementary information, Figs. S2, S5): the cytosolic (CY) domains are organized as solenoid scaffolds around a central left-handed four-helix bundle comprised of the C-terminal domains (CTD) from each subunit. The CY and transmembrane (TM) portions are hinged at the cytosolic-membrane interface via the intervening lateral (ILD) and linker (LNK) domains within each protomer of the tetrameric channel assembly (Fig. 1a; Supplementary information, Fig. S5a, b). Overall, our new structures reveal higher resolution features throughout the entire protein yielding improvements in the domain folds and loop connectivities relative to the previously reported Apo-InsP$_3$R1 structure[5] (Supplementary information, Table S2). Many side-chain densities were visible throughout the ten protein domains comprising each protomer (Supplementary information, Fig. S5c, d).

The ligand-binding pocket
The ligand-binding pocket is formed at the cleft between the β-TF2 domain (W226-V435) and the first two α-helical armadillo repeats of ARM1 (S436-K604). This region when expressed as an independent soluble entity can bind InsP$_3$ with even higher affinity than the full-length tetrameric protein. At the current resolution, the secondary structure elements and overall fold of the LBDs are consistent with the known X-ray structures.[18,19] At ~1.5 Å RMSD, the final cryo-EM based model is similar to the previously reported X-ray structures, though our model resolves a number of loops that were not previously observed (Fig. 1c; Supplementary information, Fig. S6c).

The AdA molecule was docked in the ligand-binding pocket of the AdA-InsP$_3$R1 map, and possible positions were screened based on their visual match to the density (Supplementary information, Fig. S6a, b; see Methods). The final placement of the AdA molecule had the greatest overlap with the bridging density observed between the β-TF2 and ARM1 domains. Based on the docking, AdA appears to be buttressed by two loops, formed by R265-T276 of β-TF2 and Q565-E572 of ARM1, and the ARM1 helix R504-R511 (Fig. 1b, c; Supplementary information, Table S3). AdA is uniquely oriented such that its 3″- and 4″-phosphates interact with the ARM1 domain and the adenosine moiety bridges the binding pocket interacting with the β-TF2 domain. The 2′-phosphate points inside the cleft between β-TF2 and ARM1 domains, which is opposite to the orientation of the 1-phosphate of the InsP$_3$ molecule in X-ray crystallographic structures of InsP$_3$R1[18,19] and cryo-EM structures of InsP$_3$R3.[20] To adopt a conformation suitable for ligand binding, the β-TF2 and ARM1 loops move toward the ligand, while the R504-R511 helix is relatively unchanged (Fig. 2; Supplementary information, Movie S1). While both InsP$_3$ and AdA bind to the same site, our study shows that they utilize a different set of parameters to coordinate within the ligand-binding pocket (Fig. 1c; Supplementary information, Fig. S6c). Specifically, the vicinal 3″- and 4″-phosphate groups of AdA extensively interact with residues of the ARM1 domain, while the adenine ring of AdA interfaces with residues of the β-TF2 domain on the opposite side of the ligand-binding pocket (Supplementary information, Movie S1). These complementary interactions provide the impetus for pulling the two domains towards each other, reducing the interstitial space of the binding pocket by 5 Å in the AdA-InsP$_3$R1 structure (Fig. 2a). By contrast, the 4- and 5-phosphates of InsP$_3$ interact with the β-TF2 loop and ARM1 domain, respectively, to drive the closure of the InsP$_3$-binding cleft (Supplementary information, Fig. S6c).[18,19]

Furthermore, the electrostatic potential of the ligand-binding pocket is mostly positive, though the β-TF2 ligand binding loop contributes to a small negative electrostatic patch (Supplementary information, Fig. S6c). This electrostatic potential of the ligand-binding pocket is complementary to the charge of AdA and may serve as a mechanism to localize AdA: multiple basic amino acids could facilitate ionic interactions with the negatively charged AdA phosphates while the negative electrostatic patch may aid in anchoring the positively charged adenine moiety.

Rearrangements in the ion conduction pathway
Local resolution estimates and feature visualization indicate that the TM region in both the Apo- and AdA-InsP$_3$R1 structures contains better than 3.5 Å resolution information allowing for accurate assignment of side-chains along the ion permeation pathway (Supplementary information, Figs. S2f and S5c, d). The domain-swapped arrangement of the six TM helices in InsP$_3$R1 unveiled in our previous study[5] is consistent with a long TM4-5 α-helical linker that would be inserted laterally into the cytosolic leaflet of the membrane (Supplementary information, Fig. S7). The densities on the lumenal side of the TM region are likely attributed to loops connecting TM helices. The extended lumenal TM5-6 loop is structured and harbors the pore helix (P-helix) and the selectivity filter (SF). A previously unassigned density appears between TM1 and TM2 in both maps and was assigned as a *m*embrane *a*ssociated α-helix, MA1-2 (Supplementary information, Fig. S7). MA1-2 density is likely a part of the InsP$_3$R1 protein given its contiguous connectivity with TM2 and that no additional proteins were identified in our InsP$_3$R1 preparations.[5] MA1-2 is architecturally similar to the S1″ helix observed in the InsP$_3$R3 map[20] (Supplementary information, Fig. S8a). The densities corresponding to the S1′ membrane embedded helix identified in the TM region of the InsP$_3$R3[20] (Supplementary information, Fig. S8a) were not sufficiently resolved in the InsP$_3$R1 cryo-EM density maps to make unambiguous structural interpretation. However, the presence of these membrane associated helices, which do not traverse the lipid bilayer, does not affect the transmembrane topology of either the InsP$_3$R1 and InsP$_3$R3 channels, which are topologically identical in the TM domain, and strikingly similar throughout. Moreover, TMx was recently identified in the RyR1 structure[21,22] at the same location as S1′ in InsP$_3$R3, suggesting a potential structural conservation of this feature among Ca^{2+} release channels.

The ion conduction pore of InsP$_3$R1 is shaped by four pairs of the inner TM6 and outer TM5 helices that form a right-handed bundle with a tapering pathway for ion permeation through the membrane (Fig. 3a, Supplementary information, Fig. S7). The conformation of the central TM bundle may be stabilized by stacking of aromatic residues observed at the buried interface between TM5 and TM6 helices of the same subunit (Supplementary information, Fig. S8b). In the Apo-InsP$_3$R1 structure, the pore is maximally constricted at F2586 and I2590 of the pore-lining TM6.

Cryo-EM structure of ligand-bound IP3R1 channel
G. Fan et al.

1160
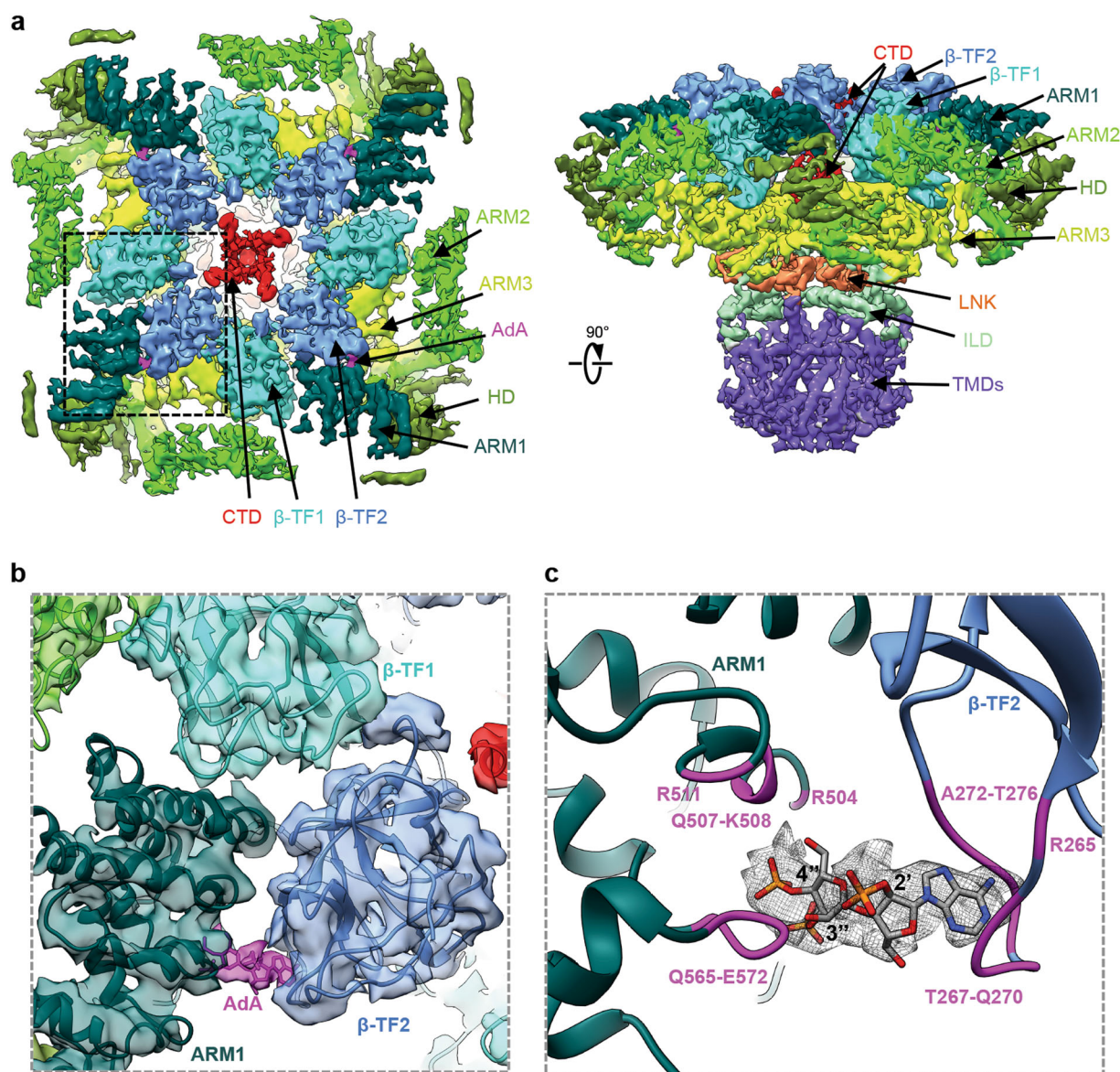
Fig. 1 The cryo-EM structure of InsP$_3$R1 channel bound with AdA. **a** The cryo-EM density map of the InsP$_3$R1-AdA complex is viewed from cytosol along its four-fold axis (left) and along the membrane plane (right). The map is filtered to 4.1 Å and corrected with a temperature factor of −100 Å^2. The domains within each protomer are delineated by different colours. Densities corresponding to AdA are coloured magenta. **b** Zoomed-in view of the AdA density present in the ligand-binding pocket. AdA-InsP$_3$R1 structure is overlaid on the corresponding density map and coloured by domain; the AdA molecule is fit in the density adjoining the LBDs. **c** AdA molecule is shown in the InsP$_3$R1 binding pocket and is overlaid with densities (mesh) from the difference map (4σ). Residues within 5 Å distance from the docked AdA molecule are labeled and coloured magenta

Here, the side-chains form two hydrophobic rings near the cytosolic leaflet of the ER membrane (Fig. 3a, b); the minimum distances across the ion conduction pathway at F2586 and I2590 are 4.5 Å and 6 Å, respectively (Fig. 3c, d), which will preclude the passage of hydrated cations (e.g., Ca^{2+}, Na$^+$ and K$^+$). Thus, our Apo-InsP$_3$R1 structure is in a non-conductive closed state with F2586 and I2590 of TM6 serving as the pore gate. This assignment is consistent with our previous cryo-EM studies[5] and supported by multiple mutagenesis and electrophysiological studies previously demonstrating that mutations in this region abolish channel conductance.[23,24] Hence, conformational rearrangements that lead to pore dilation are necessary to allow for ion conductance of InsP$_3$R upon activation.

Indeed, in the AdA-InsP$_3$R1 structure the TM helices exhibit significant structural changes (Supplementary information, Fig. S7b). Structural rearrangements of TM helices are characterized by the changes to the central helical axis tilt with respect to their orientations in the Apo-state. The TM6 appears to have three segments (TM6a, TM6b, TM6c) with separate tilt axes that together form the ~ 70 Å long helix. The change in tilt angle of these three segments is different with the greatest change in tilt axis within the TM6b segment, which contains the residues comprising the gate. The movements of TM6 result in a bulge away from the 4-fold central axis between I2580 and M2576 and F2575 (Fig. 3e). The TM6 conformational changes observed in the AdA-InsP$_3$R1 structure cause the aromatic ring of F2586 to rotate ~ 90° from the plane normal to the ion conduction pathway. This results in the expansion of the corresponding hydrophobic ring to ~ 7.5 Å while the hydrophobic seal at I2590 dilates minimally (Fig. 3a–d).

Beyond the gate, the ion conduction pathway widens substantially into the cytoplasmic vestibule, where the R2597

Cryo-EM structure of ligand-bound IP3R1 channel
G. Fan et al.

1161
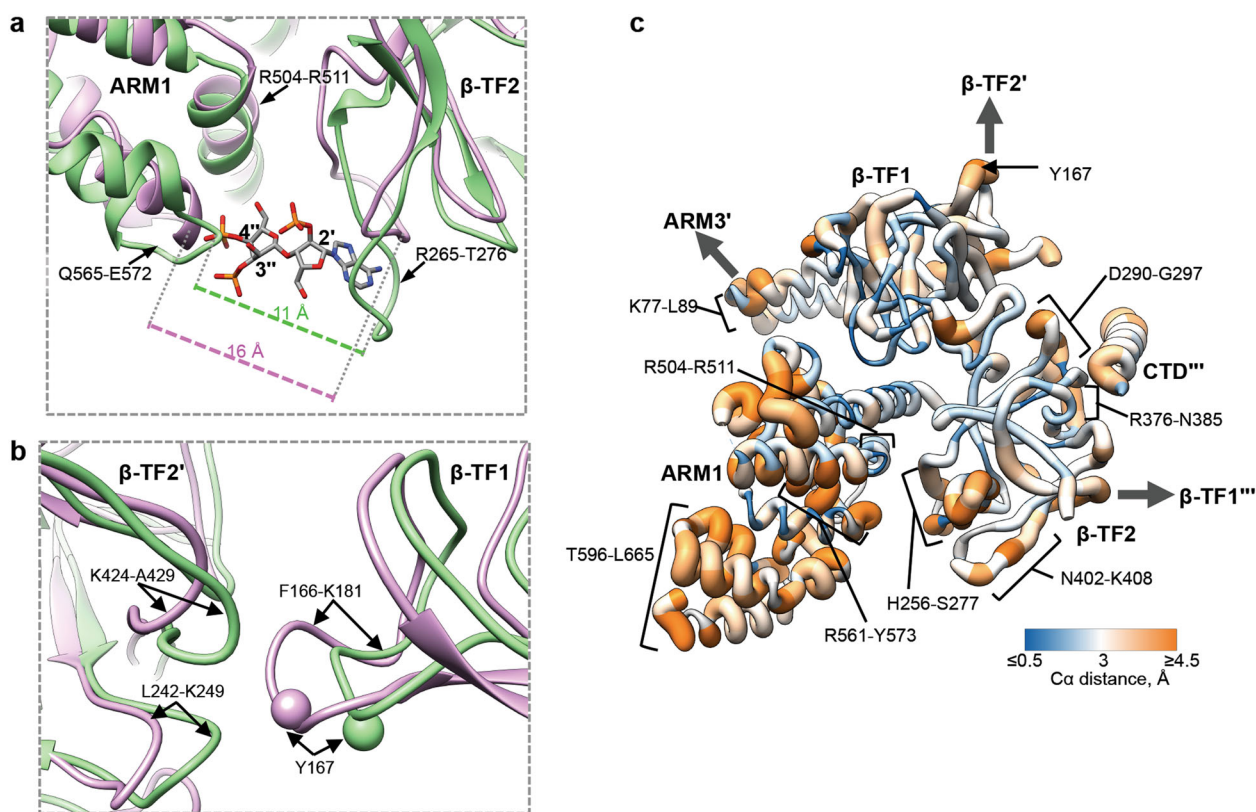
Fig. 2 Structural rearrangements in the ligand-binding pocket of InsP₃R1. **a** Shown is an overlay of ribbon diagrams of the ARM1 and β-TF2 domains from Apo-InsP₃R1 (light purple) and AdA-InsP₃R1 (green). The structure of AdA molecule is colour-coded by element (phosphorous - orange; oxygen - red; nitrogen - blue; carbon - grey) and shown within the binding pocket; 2'-, 3''- and 4''- phosphates are labeled. Distances between Cα atoms at the narrowest point within the ligand binding pocket for AdA-bound (between T266 and K569) and Apo-InsP₃R1 (between G268 and K569) are indicated. **b** Overlay of the AdA- (green) and Apo- (light purple) InsP₃R1 structures zoomed in at the β-TF1/β-TF2' interface. Y167 is depicted as a sphere. **c** The Cα RMS deviations calculated between Apo- and AdA-bound structures are shown in the AdA-bound LBD structure colour-coded based on RMS deviation - ribbon color/thickness denotes lowest RMSD (blue/thinnest) to highest RMSD (orange/thickest). The most variable residues contributing to intra- and inter-domain contacts are labeled. Wide arrows point to the interacting domains of neighboring subunits. The prime symbol (') is used to differentiate subunits

residue is positioned (Fig. 3a, b; Supplementary information, Fig. S9a). Here, we propose a network of interactions centered around the R2597 that could play a role in transmitting signals to the gate, in part, through an interaction between neighboring TM6 helices. R2597 is highly conserved among both InsP₃R and RyR channels, and mutations R2597A, R2597K and D2591A substantially diminished the channel function, supporting importance of these identified interactions in the cytosolic pore vestibule.[24] Additionally, the TM4-5 linker between the central pore helices and the bundle of peripheral TM1-TM4 helices, is positioned in proximity to the TM6 helix at a TM6-TM6' interface (Supplementary information, Figs. S7, S9a). In the AdA-InsP₃R1 structure TM4-5 undergoes conformational changes that may alter its interaction with TM6 (Supplementary information, Movie S2). Movement of TM4-5 has been proposed to relieve the steric constriction of the gate allowing it to transition from closed to open conformation.[25,26]

The central TM5 and TM6 helices provide the structural framework that positions the P-helix and the interconnecting loops shaping the lumenal vestibule, which may function as a cation accumulating reservoir positioned before the SF (Figs. 3a, 4), a property shared by other cation channels.[27] The SF of InsP₃R1 is formed by the conserved residues G2546-V2552 (Fig. 4a). Notably, the lumenal vestibule in Apo-InsP₃R1 structure are large enough to accommodate hydrated ions and does not constitute a barrier that precludes ion passage. In the AdA-InsP₃R1 structure, the P-loop undergoes structural rearrangements

resulting in both a physical constriction and an increase in the electronegative potential in the SF (Fig. 4b–d). The separation between Cα atoms from two opposing subunits narrows from 12 Å to 8.5 Å before the entrance to the central hydrophobic cavity. This suggests, that in AdA-InsP₃R1 a Ca²⁺ ion might be able to pass through the filter by, at least partially, displacing its hydration shell, given that the diameter of hydrated Ca²⁺ is 8–10 Å.[28,29]

The ligand-induced rearrangements in the SF may confer a weak selectivity of Ca²⁺ over monovalent cations ($P_{Ca}/P_K \sim 6$–8) in InsP₃R channels analyzed in electrophysiological experiments. The modest selectivity of the InsP₃R1 channel implies that the SF is rather permissive in the presence of other cations, such as Na⁺ or K⁺.[1,30,31] In the AdA-InsP₃R1 structure, the positively charged surface preceding the constriction of the SF may serve to focus cations along the ion conduction path via electrostatic repulsion, and together with the physical and chemical properties of the SF would provide the basis for the screening of permeant cations. The Ca²⁺ ion being more electropositive than Na⁺ or K⁺, would be better coordinated and bind more tightly in the SF. This may prevent entrance of other monovalent cations to the permeation path, thereby providing a plausible mechanism for modest ion selectivity.[1,30-32] Noteworthy, in vivo unidirectional Ca²⁺ flux via InsP₃Rs to the cytosol is largely driven by the high Ca²⁺ concentration in the lumen, ensuring rapid occupancy of the SF. Overall, the importance of rearrangements in the lumenal vestibule is supported by previous mutagenesis within the SF, which showed that D2551A inactivated InsP₃R1 channel function

Cryo-EM structure of ligand-bound IP3R1 channel
G. Fan et al.

1162
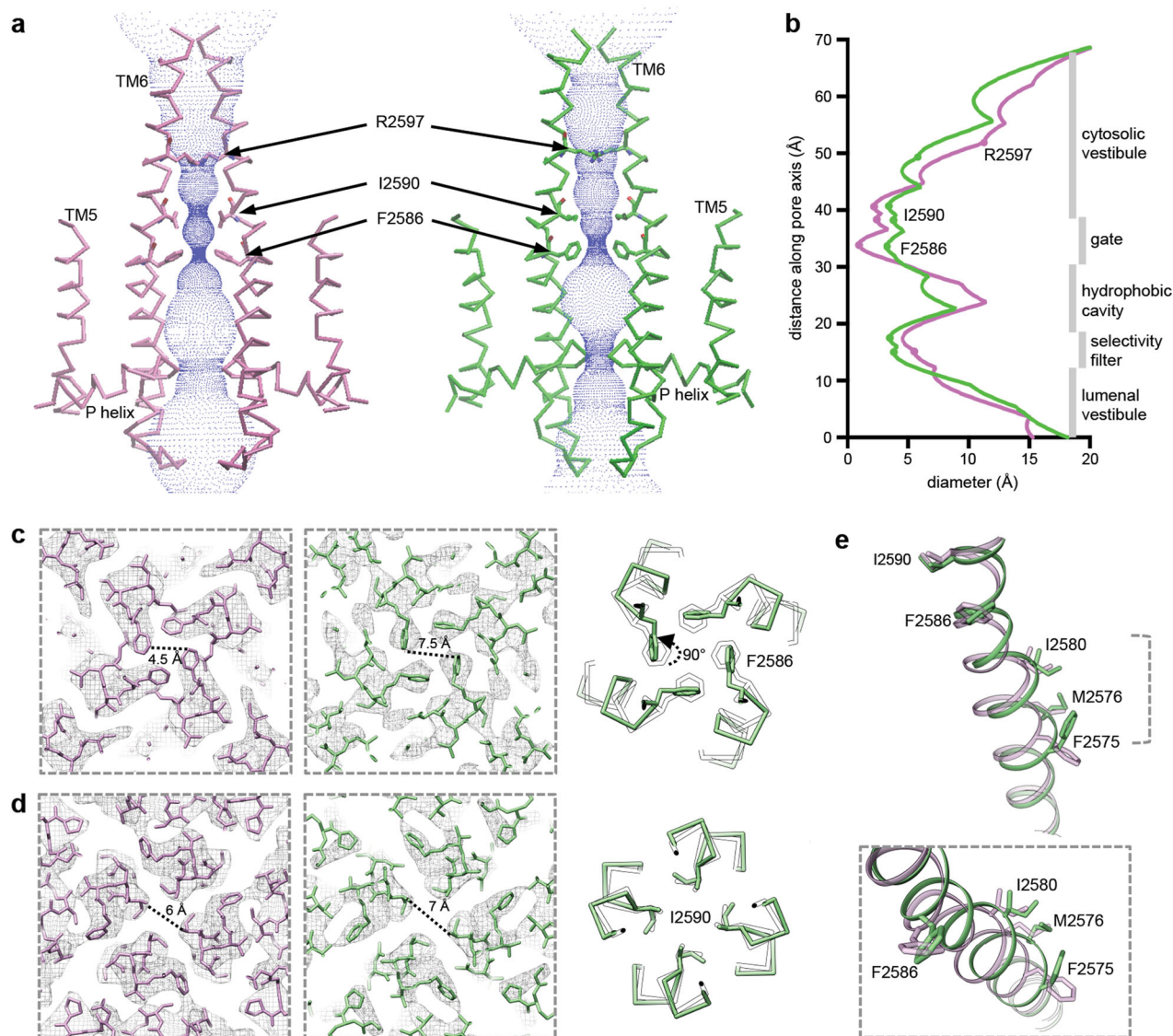
Fig. 3 Conformational changes in the ion conduction pathway upon ligand binding. **a** Solvent-accessible pathway along the pore mapped using the program HOLE[75] for Apo- (light purple) and AdA-bound (green) InsP₃R1. A series of residues within the ion conduction pathway of the channel pore are labeled. **b** Comparison of pore diameter for Apo- (light purple) and AdA-bound (green) InsP₃R1. **c–d** Sections of density maps perpendicular to the four-fold axis at the position of F2586 (**c**) and I2590 (**d**) are shown overlaid with their corresponding models and viewed from the cytosol; Apo-InsP₃R1 model is shown in light purple, AdA-InsP₃R1 is shown in green; distances between the sidechains from two opposing TM6 helices are indicated; corresponding side-chain rotations are indicated in the right panels. **e** Zoomed-in views of the bulge in TM6 seen in AdA-InsP₃R1 (green) overlaid on TM6 from Apo-InsP₃R1 (light purple). The lower panel represents a ~ 40° rotation in view from the upper panel
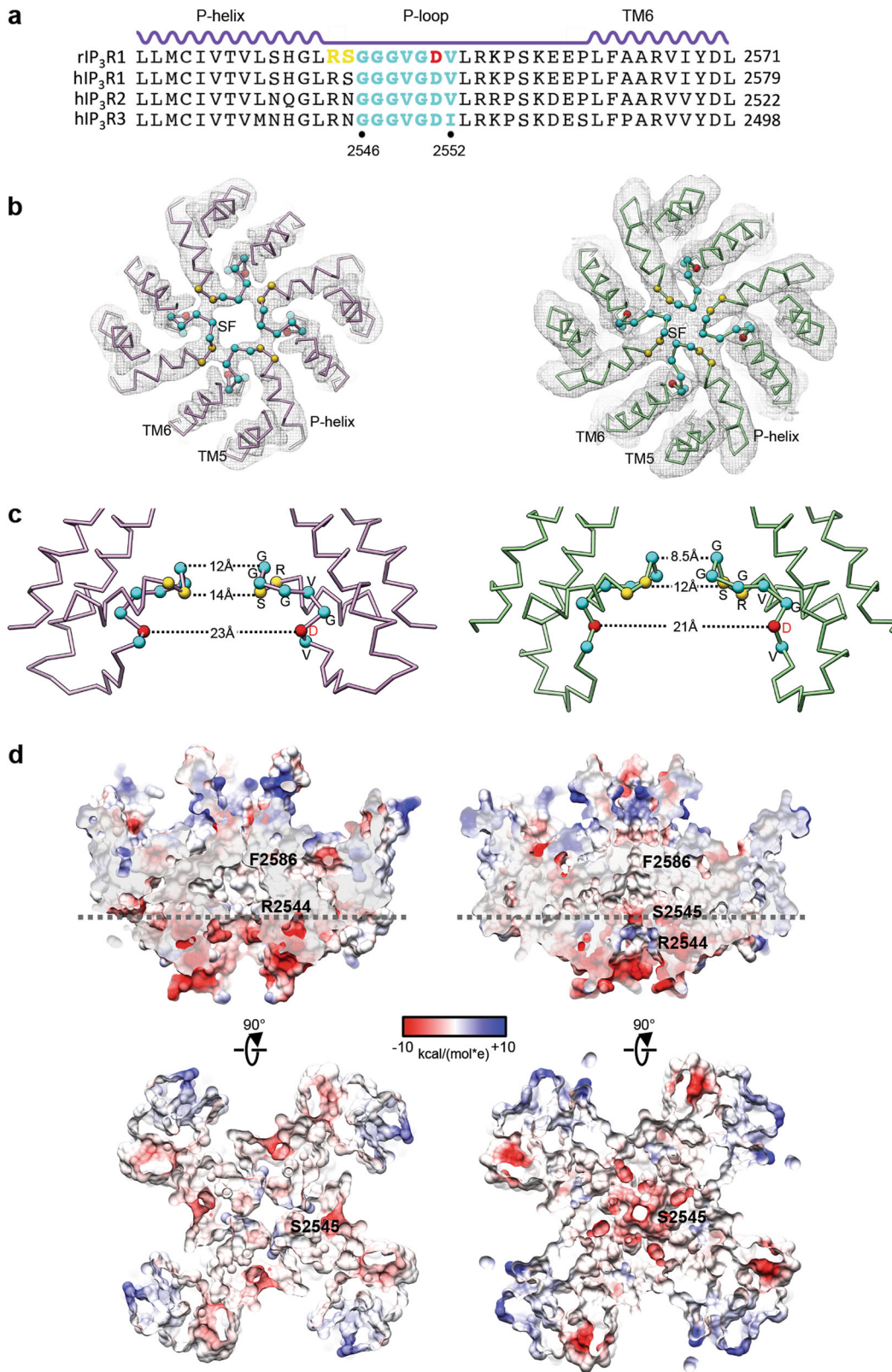
and D2551E exhibited altered cation selectivity and was nonselective for Ca²⁺ over K⁺, with unchanged ion conductance of both cations.[33]

Ligand-mediated allosteric network
In comparing the AdA- and Apo-InsP₃R1 structures, striking conformational rearrangements in inter- and intra-subunit interfaces coincident with AdA-binding are evident and likely play a role in propagation of ligand-evoked signals towards the ion conduction pore in order to open the channel gate (Supplementary information, Movies S1, S2). The LBDs (β-TF1, β-TF2 and ARM1) are contained within each InsP₃R1 subunit and form a triangular architecture comprising an apical portion of the cytoplasmic region, similar to that seen in the earlier crystal structures of the isolated LBDs (Supplementary information, Fig. S10a).[18,19] Binding of AdA within the ligand-binding pocket

induces global rigid body movements of all three LBDs. Ligand binding in the tetrameric channel results in a 5 Å closure of the cleft between the ARM1 and β-TF2 domains (Fig. 2a), while β-TF1 acts as a pivot for the concerted movement of ARM1 and β-TF2. The ARM1/β-TF1/β-TF2 angle decreases whereas the β-TF1/β-TF2/ARM1 angle increases (Supplementary information, Fig. S10b). These cooperative changes in the relative orientations of LBDs, combined with subtle changes in their internal structure, render the ligand-binding pocket amenable for capturing ligand.

Not restricted to intra-subunit interactions, changes of LBDs within one subunit are propagated to the interfacial elements between adjacent subunits. Notably, residues at the interface between the β-TF1 and β-TF2 domains from the adjacent subunits undergo conformational changes involving Y167, which is essential for Ca²⁺-release activity (Fig. 2b, c; Supplementary information, Movie S1).[34] Additionally, the helix–turn–helix

Cryo-EM structure of ligand-bound IP3R1 channel
G. Fan et al.

1163

a


```
                P-helix                    P-loop              TM6
rIP₃R1  LLMCIVTVLSHGLRSGGGVGDVLRKPSKEEPLFAARVIYDL 2571
hIP₃R1  LLMCIVTVLSHGLRSGGGVGDVLRKPSKEEPLFAARVIYDL 2579
hIP₃R2  LLMCIVTVLNQGLRNGGGVGDVLRRPSKDEPLFAARVVYDL 2522
hIP₃R3  LLMCIVTVMNHGLRNGGGVGDILRKPSKDESLFPARVVYDL 2498
                        2546    2552
```

b

c

d

structure (S67-L110) of β-TF1 rotates and moves toward the ARM3 domain of the adjacent subunit (Figs. 2c, 5a). To compensate, the interfacial loop of ARM3 (S2013-Y2024) undergoes a modest motion combined with a slight structural rearrangement. Of note,

one of the ARM3 interfacial loops carries a putative ATP-binding site (ATPB) that is present in all three InsP₃R isoforms.[1,35–37] While this loop undergoes conformational changes in our structure, earlier studies showed that this putative ATP binding site (ATPB) is

Cryo-EM structure of ligand-bound IP3R1 channel
G. Fan et al.

1164

Fig. 4 Detailed views of the selectivity filter in InsP₃R1. **a** Sequence alignment for the P-loop region of selected InsP₃R channels; the secondary structure elements are given above sequences; highly conserved residues within the signature sequence of the SF are coloured cyan; residues undergoing significant conformational changes are coloured yellow; D2551 within the SF, for which mutations can abolish Ca²⁺ conductance, is colored red; **b** EM densities with the corresponding models for the SF of Apo- (light purple) and AdA-InsP₃R1 (green) are viewed from the cytosolic side. Cα atoms within the SF are depicted as spheres with the same colour code as in (**a**). **c** The SF (wire representation) from two opposing subunits is viewed from the side in Apo- (light purple) and AdA-InsP₃R1 (green); distances between Cα atoms (spheres, colour-coded as in (**a**)) along the SF are indicated; **d** The surface electrostatic potential in the SF. Top panels show cross-sections along the 4-fold axis through the ion conduction pathway in Apo- (left) and AdA-InsP₃R1 (right); lumenal entrance at the bottom. Bottom panels slices through the channel pore perpendicular to the 4-fold axis at the positions indicated with dashed lines in upper panels (viewed from lumen)

only involved in ATP regulation of InsP₃R2, not in InsP₃R1 or InsP₃R3.[38–41]

Furthermore, the β-TF2 domain is located in close proximity to the CTD of the adjacent subunit (Fig. 5b; Supplementary information, Movie S1).[5] It follows then that the ligand-evoked structural changes of β-TF2 trigger a pronounced rotation of the CTD helix and this motion propagates through the CTD helix, thereby directly coupling remote but functionally coordinated domains (Supplementary information, Movie S2, Fig. S3b). Importance of this structural coupling was predicted based on earlier biochemical studies where deletion of the last 60 residues of InsP₃R1 or the creation of a chimeric channel, comprised of the TMD and CTD of RyR1, which lacks the coiled-coiled feature, and the cytosolic domains of InsP₃R1, greatly impaired channel function.[19,25]

The CTD helical bundle is one of the most striking and reproducible features in our reconstructions regardless of functional state. Despite the similar overall architectural arrangement of both type 1 and type 3 InsP₃Rs, the CTD bundle is not resolved in any of the recently reported cryo-EM maps of InsP₃R3.[20] Given the lack of any functional characterization of the purified InsP₃R3 in that study, it is conceivable that the channel might not retain structural coupling between the LBDs and TMDs, which is critical for the channel activation based on our observations of InsP₃R1.

Based on our structures, the ILD/LNK sandwich, which resides near the cytosolic face of the membrane in the tetrameric channel assembly, represents the sole direct structural link between the cytoplasmic and transmembrane domains (Fig. 6). Furthermore, the CTD is directly connected to the LNK, thus enabling a mechanism for cooperative communication between the ligand-binding and transmembrane domains. Notably, portions of the ILD/LNK sandwich move horizontally away from the four-fold axis following the binding of AdA (Supplementary information, Movie S3). Mutations within the first two strands of the ILD domain support the mechanism of signal transduction through the assembly formed by the interleaving ILD and LNK domains at the membrane cytosol interface.[42] However, the ILD conformation in AdA-InsP₃R1 is quite different from that observed in the crystal structure of an isolated cytoplasmic portion of the protein, which lacks the molecular constraints provided by the tetrameric assembly of the full-length InsP₃R1.[42] The LNK domain contains a putative Zn²⁺ finger motif that is structurally conserved among the related families of InsP₃R and RyR proteins.[5,20,21,43,44] While some evidence points to regulation of RyR2 by Zn²⁺,[45,46] it has yet to be unambiguously demonstrated that Zn²⁺ binds and regulates InsP₃R channels.

The putative Ca²⁺-sensor region containing conserved E2101[47,48] sits at the ARM3-LNK interface that undergoes modest conformational changes in our experimental conditions (Supplementary information, Movie S3). Alignment of 3D structures of InsP₃R1 with related intracellular Ca²⁺ release channels reveals a conservation of the protein fold within this region, containing a structurally conserved putative Ca²⁺-binding site in the same location[6,20,21] (Supplementary information, Fig. S9b, c). While the buffer conditions for the AdA-InsP₃R1 structure include Ca²⁺, the

cation concentration was targeted for the channel activation rather than saturation of the Ca²⁺ binding sites, and as a result the densities that could be attributed to Ca²⁺ ions were not observed in the AdA-InsP₃R1 map.
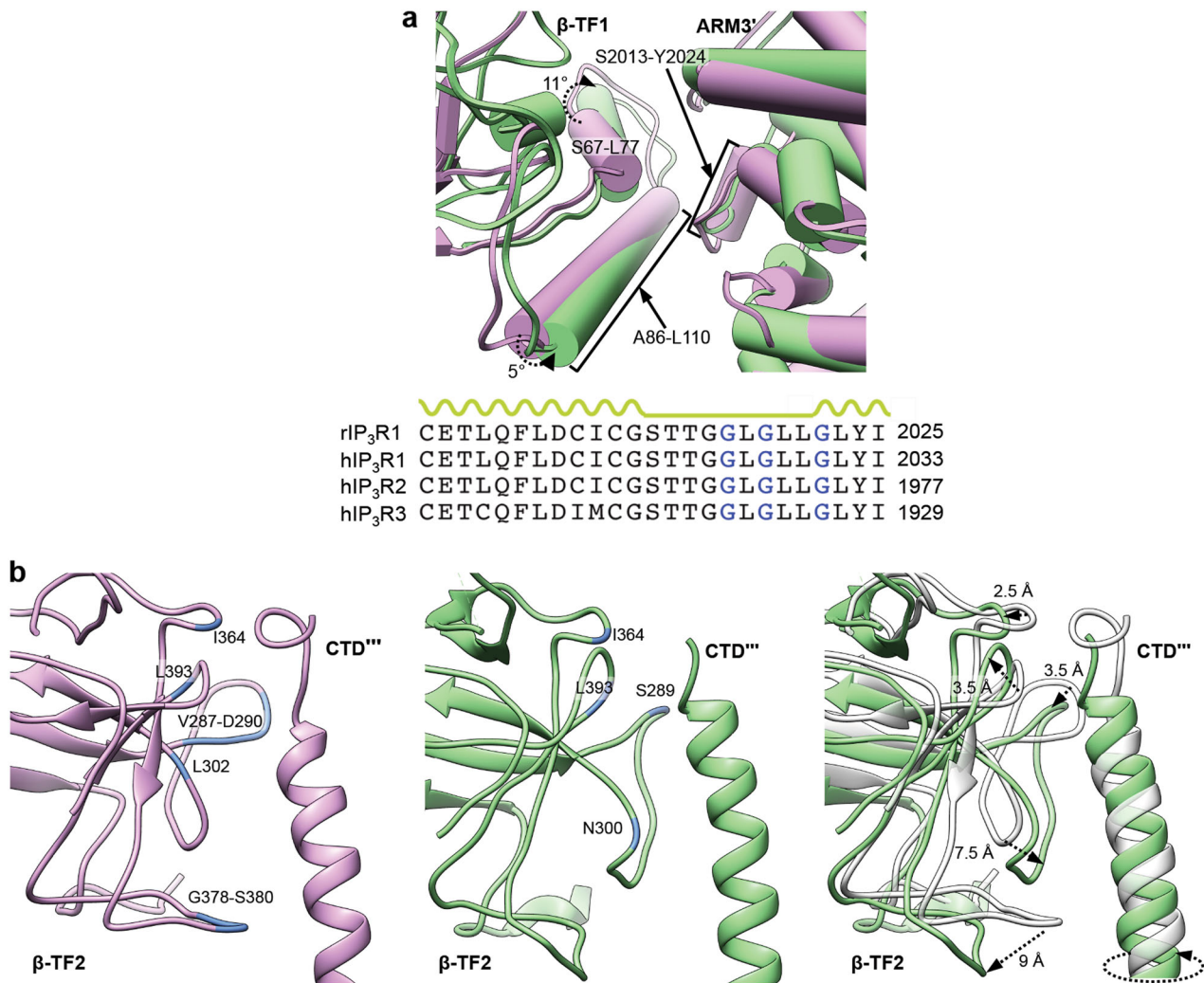
DISCUSSION

The present study describes 3D structures of neuronal type 1 InsP₃R channel with and without the agonist bound. These structures bring into focus molecular features of the ligand binding domains and ion conduction pathway, in which conformational changes are required for activation of the channel gate that enables passage of Ca²⁺ ions.

Conformational sensitivity of InsP₃R to ligands is a fundamental property of this ion channel underlying its fascinating ability to function as signal transducer. While binding of both AdA or InsP₃ to InsP₃R causes activation of the channel, it is conceivable that the differential interactions of ligands within the LBDs would confer the unique properties within the LBD that allow AdA to bind with greater affinity and potency.[9,10,14] This view is supported by earlier studies with synthetic analogues of AdA and InsP₃.[9,17] Our analysis suggests that the 3″- and 4″- phosphate groups and adenine moiety are important determinants of the increased affinity and high-potency of AdA for InsP₃R. Our structure reveals that the adenine moiety of AdA interacts with residues of β-TF2 (Fig. 1c; Supplementary information, Fig. S6c, Table S3) rather than with the ARM1 as previously proposed.[9] Furthermore, the 2′-phosphate does not make strong contact with the β-TF2 domain, suggesting that it likely does not contribute to the high-affinity binding of AdA. This is consistent with earlier functional and ligand-binding studies demonstrating that AdA analogues lacking adenine, but retaining the 2′-phosphate, typically have a binding affinity similar to InsP₃.[9,16]

Our study supports the concept of long-range conformational changes that propagate from ligand-binding N-terminal domains towards the ion-conducting pore through an allosteric network of specific inter- and intra-subunit contacts (Fig. 7). This study visualizes the binding of AdA at the cleft between the β-TF2 and ARM1 domains that promotes conformational changes in the ligand-binding domains. In turn, this triggers concerted rearrangement of the cytoplasmic solenoid structure organized around the central CTD helical bundle. The interfacial region formed by the ILD and LNK domains undergoes lateral movements that appear to be mechanically connected to pore opening, whereby changes in the ILD/LNK interface generate a force on the TMD via their connecting linkers. As a result, the TMDs undergo rearrangement with the SF adopting an optimal conformation favorable for screening and conduction of cations. The resulting rearrangement in the pore forming helical bundle leads to dilation of the hydrophobic constrictions at the crossing of four TM6 helices.

A surprising finding is that the hydrophobic rings at F2586 and I2590 are not sufficiently dilated in the presented AdA-InsP₃R1 structure to allow a hydrated Ca²⁺ ion to pass through the channel (Fig. 3). Nevertheless, the substantial ligand-evoked conformational changes observed in the ion conduction pore suggest that we visualized the channel in an intermediate gating state. There are a few entangled issues related to the complex

Cryo-EM structure of ligand-bound IP3R1 channel
G. Fan et al.

1165

rIP₃R1 C E T L Q F L D C I C G S T T G G L G L L G L Y I 2025
hIP₃R1 C E T L Q F L D C I C G S T T G G L G L L G L Y I 2033
hIP₃R2 C E T L Q F L D C I C G S T T G G L G L L G L Y I 1977
hIP₃R3 C E T C Q F L D I M C G S T T G G L G L L G L Y I 1929

Fig. 5 Inter-subunit contacts within cytoplasmic region. **a** Superimposition of interfaces between β-TF1 and ARM3′ domains in AdA-bound (green) and Apo- (light purple) InsP₃R1 structures; helices are rendered as cylinders. The lower panel shows the ATP-binding consensus (GXGXXG, indicated in blue) within the ARM3 domain. **b** Interface between β-TF2 and CTD′′′ domains in AdA-bound (green) and Apo- (light purple) InsP₃R1 structures is shown in view parallel to the membrane plane. β-TF2 residues within 5 Å of the CTD are coloured blue and labeled. Right panel shows the overlay of AdA- (green) and Apo- (grey) InsP₃R1 models. Notable structural changes are indicated. In the AdA-InsP₃R1, the CTD helix exhibits pronounced rotation compared to its position in the Apo-structure

activation kinetics of InsP₃R channel that might impact homogeneity of the ligand-bound InsP₃R1 preparations on an EM grid.

Even under the most favorable circumstances the maximum open probability reported for InsP₃R1 approaches 80% since openings are interrupted by brief closures.[49] The key question is what causes these rapid closures? One set of electrophysiological observations shows that InsP₃R continuously exposed to InsP₃ switches to some type of non-conducting state.[50] However, this observation is challenged by other studies.[51,52] While neither satisfactorily accounts for their differences, it may reflect some intrinsic property of InsP₃R, such as desensitization or inhibition that inexorably follows InsP₃ binding. Moreover, InsP₃R1 exhibits 'modal gating' where the channel switches between kinetically distinct states even in the presence of saturating concentrations of ligand.[49] This phenomena might reflect the rapid flickering of a gate within a liganded channel rather than ligand-binding events.[53]

The recent studies of concatenated InsP₃R1 raise an additional possibility that the channel opens only when all four ligand-binding sites are occupied.[54] This possibility is somewhat contentious given that it would require substantial increase in

InsP₃ concentration to achieve appreciable activity of InsP₃R channels in vivo.[55] Furthermore, it is evidenced that lipids influence structural dynamics and molecular requirements for RyR channel gating.[56] Thus, it is conceivable that the activation kinetics of InsP₃R1 in the aqueous environment maintained in the vitrified sample is different from that in lipid bilayer. While our structures begin to establish a paradigm for ligand-mediated InsP₃R gating, further high-resolution studies of different ligand-bound states will be necessary to distill these issues.

MATERIALS AND METHODS
Protein purification and ligand-binding assay
All biochemical reagents were obtained from Sigma-Aldrich, Co. unless otherwise stated. Detergent-solubilized InsP₃R1 was purified from rat cerebellum as described in our earlier studies.[5,57] To assess the ability of purified InsP₃R1 to bind AdA, we carried out equilibrium-competition ³H-InsP₃ binding assays of cerebellar microsomal membranes and detergent purified receptors in buffer closely representing cryospecimen conditions. For microsomal membranes (100 μg), ³H-InsP₃ (PerkinElmer or American

Cryo-EM structure of ligand-bound IP3R1 channel
G. Fan et al.

1166
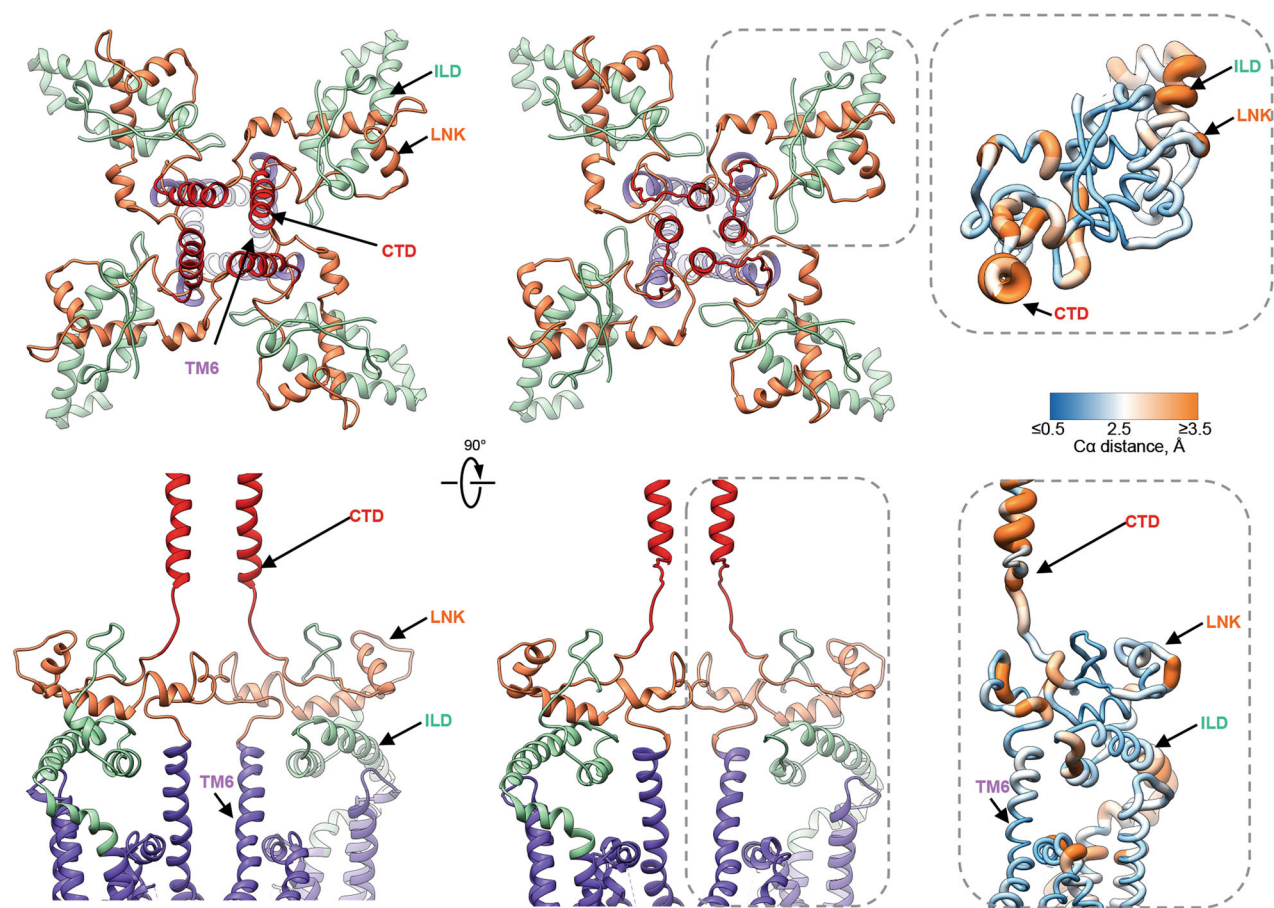
Fig. 6 Domain rearrangements at the cytosolic-membrane interface. Two orthogonal views of domains at the cytosolic-membrane interface in the Apo- (left) and AdA-bound (right) InsP$_3$R1 structures (colour-coded by domain). Structural differences are notable in the CTD helices (red), which are connected to the LNK domain (orange). Ligand-triggered conformational changes are ultimately funneled to the TMDs (purple) through the interface comprised of the ILD/LNK sandwich. The lower panels show two opposing subunits for clarity. Inserts show zoomed-in views (indicated with dashed-lines) of domains from one subunit of AdA-InsP$_3$R1 that are colour-coded based on the Cα RMS deviations calculated between Apo- and AdA-structures: ribbon color/thickness denotes lowest RMS (blue/thinnest) to highest RMS (orange/thickest) deviations

Radiolabeled Chemicals, Inc.) binding (5 nM) was measured in 200 μL of 50 mM Tris-HCl pH7.4, 1 mM EDTA, 100 mM NaCl, 2 mM DTT in the presence of various concentrations of either InsP$_3$ or AdA (Calbiochem). After a 5 min incubation at 4°C, samples were rapidly vacuum filtered through Whatman GF/F filters and washed once with 2.5 mL ice-cold water. Non-specific binding was determined by addition of 10 μM InsP$_3$ or 1 μM AdA. For purified InsP$_3$R (3–5 μg), ^{3}H-InsP$_3$ binding (5 nM) was measured in 200 μL of 50 mM Tris-HCl pH7.4, 1 mM EDTA, 100 mM NaCl, 2 mM DTT, 0.4% CHAPS, 0.1 mg/mL BSA in the presence of various concentrations of AdA. After a 5 min incubation at 4°C, 50 μL of 50 mg/mL γ-globulin and 500 μL of 30% polyethlyenegycol (PEG) 8000 was added. The mixture was incubated at 4°C for 10 min and filtered and washed, as described above. Radioactivity was determined by liquid scintillation counting upon addition of 5 mL Ultima Gold scintillation cocktail (PerkinElmer). Non-specific binding was measured in the presence of 1 μM AdA. Graphs and non-linear regression to determine IC$_{50}$ were generated in Prism 7.0 (Graphpad) and each curve is representative of three independent experiments with error bars denoting SEM (Supplementary information, Fig. S1b, c).

Cryo-specimen preparation and cryo-EM imaging
For cryo-EM analysis, the purified InsP$_3$R1 (0.1 mg/mL) in 50 mM Tris-HCl buffer (pH 7.4) containing 150 mM NaCl, 2 mM DTT, 1 mM

EDTA, 0.4% CHAPS, protease inhibitors[57] was incubated either with 100 nM of AdA and 300 nM of Ca^{2+} (ligand-bound state) or with 1 mM EGTA (Apo-state, no ligands added) for 60 min on ice. Vitrification of the InsP$_3$R1 samples was performed as described earlier.[5,57] The filter paper (Whatman 597) with the least content of Ca^{2+} (< 8 μg/g, per communication with GE Health/Watman Inc.) was used during the vitrification procedure. Amount of Ca^{2+} from the filter paper was taken into account when final free Ca^{2+} concentrations were determined using MaxChelator (http://maxchelator.stanford.edu/oprog.htm). Images of ice-embedded InsP$_3$R1 in the Apo- and ligand-bound states were acquired using Tecnai G2 Polara electron microscope (Thermo Fisher Scientific, Inc.) operated at 300 kV under low-dose conditions. Images were recorded on a K2 Summit direct detector (Gatan, Inc.) in super-resolution counting mode. Data sets were collected at a nominal magnification of 31,000 × corresponding to a calibrated physical pixel size of 1.26 Å on the specimen scale corresponding to super-resolution pixel size of 0.63 Å. The dose rate on the camera was 10 electrons/physical pixel/second. The total exposure time of 6 s (for Apo-state) and 7 s (for ligand-bound state) was fractionated into 30 and 35 subframes, respectively, each with 0.2 s exposure time, giving the total accumulated dose of 38 electrons Å^{-2} and 44 electrons Å^{-2} at the specimen plane, respectively. Images were acquired using SerialEM[58] at a defocus range of 0.8 to 3.5 μm (Supplementary information, Table S1).

Cryo-EM structure of ligand-bound IP3R1 channel
G. Fan et al.

1167
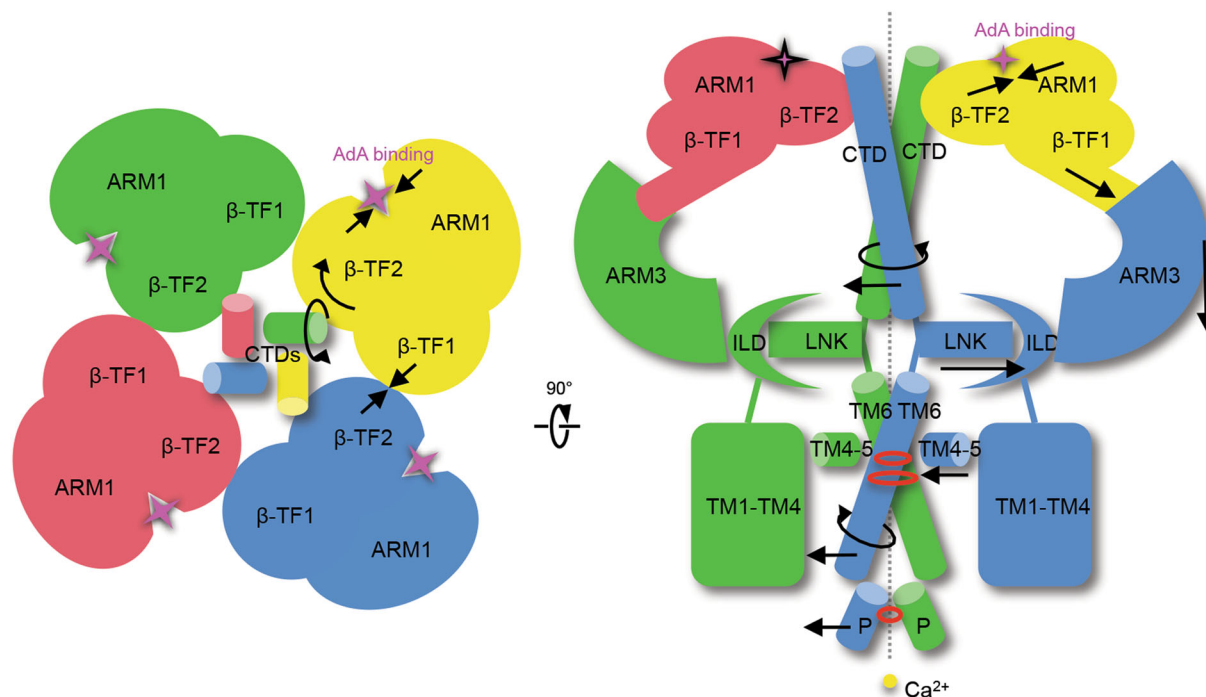
Fig. 7 Schematic of ligand-induced conformational changes underlying activation of InsP$_3$R1. Top view of the channel along the 4-fold axis from the cytosolic side (left panel). Depicted are the LBDs and CTDs for each InsP$_3$R1 protomer coloured by subunit. Section of tetrameric InsP$_3$R1 through its 4-fold axis is viewed parallel to the membrane plane (right panel); regions of constriction and SF are indicted with red circles, Ca^{2+} ion - yellow sphere. Ligand-evoked domain motions are indicated with arrows. Presumably, conformational changes evoked by binding of AdA between the β-TF2 and ARM1 domains are propagated via several inter-subunit interfaces (β-TF1/β-TF2, CTD/β-TF2 and β-TF1/ARM3) in the cytoplasmic solenoid structure to the ILD/LNK assembly that can exert force directly on the TMDs to open the channel gate

Image processing

Image processing was performed independently using RELION and EMAN2. Both software packages achieved near-atomic resolution in large regions of the structure. However, based on a local resolution assessment performed independently for each map, different domains were better resolved by each software package. To avoid human bias and extract the most information from each reconstruction the final interpreted maps were locally filtered averages of the EMAN2 and RELION maps for both Apo- and ligand-bound states. To combine the two maps, a local resolution filter, based on a windowed FSC local resolution assessment, was performed independently on the two maps. The two locally filtered maps were then averaged together. The local filtration determines the contribution of each map at each resolution in each region of the final composite map, permitting each map to dominate in regions where better self-consistency was obtained during refinement. We can only hypothesize the cause for the differing resolution distribution between the software packages, but it likely relates to the fact that RELION operates purely in Fourier space whereas EMAN uses a hybrid of real and Fourier space operations. Neither method is intrinsically superior, but the two techniques distribute residual noise and artifacts in different ways in the final reconstruction.

Image processing and 3D reconstruction in RELION. For both Apo-InsP$_3$R1 and AdA-InsP$_3$R1 datasets, the raw image stacks were binned 2 × 2 by Fourier cropping resulting in a pixel size of 1.26 Å. Each image stack was subjected to motion correction using 'Motioncorr' and the motion-corrected frames were summed using frames 2-17 to a single micrograph for further processing (Supplementary information, Fig. S2a, b).[59] We used 'e2eval-image.py' in EMAN2[60] to select 8,450 micrographs from a total of 9,823 micrographs (Apo) and 9,455 micrographs from a total of 14,686 micrographs (ligand-bound) for subsequent processing.

207,914 (Apo) and 191,646 (ligand-bound) particles were selected using 'e2boxer.py' (Supplementary information, Table S1). Defocus and astigmatism were determined for each micrograph using CTFFIND3.[61] 144,194 particles of Apo-InsP$_3$R1 and 179,760 particles of AdA-InsP$_3$R1 were selected after 2D classification and subjected to further 3D classification in RELION.[62] Our previously published map (EMDB #6369) was low pass filtered to 60 Å resolution and used as a starting model for the refinement. Four-fold symmetry was applied during all refinement steps that were performed as described previously.[5,6] In the RELION post-processing step a soft mask was calculated and applied to the two half-maps before the Fourier shell correlation(FSC) was calculated. B-factors were estimated (−300Å^2 and −170Å^2, for Apo- and AdA-bound maps, respectively) during post-processing procedure in RELION and applied to the map sharpening step. The resolutions for the final 3D reconstructions using standard 3D refinement approach were 3.9 Å for Apo-InsP$_3$R1 (from 65,438 particles) and 4.5 Å for ligand-bound InsP$_3$R1 (from 179,760 particles) based on the gold standard FSC 0.143 criteria (Supplementary information, Fig. S2d).[63,64] The corresponding particle orientation distributions are shown in Supplementary information, Fig. S2c. Local resolution variations were estimated using ResMap[65] (Supplementary information, Fig. S2f). The ligand-bound dataset was further processed using focused classification and 3D refinement strategy as detailed in the following section.

Focused 3D classification in RELION. To assess structural variability of the AdA-InsP$_3$R1 particle population, we performed a 3D classification focused on the LBDs: β-TF1, β-TF2 and ARM1. First we made 4 copies of each particle, one for each of the 4 symmetry-related orientations. Next, a mask with a soft edge extension ('relion_mask_create') was applied to one LBD region within the initial AdA-InsP$_3$R1 density map from RELION (Supplementary information, Fig. S3). The modified map with a masked

out LBD region from one subunit was re-projected in 2D using the modified euler angles for each particle from the expanded data set. The generated projection images were subtracted from the corresponding particles in the expanded data set to generate a new data set, which includes only the masked region of each particle. The new data set was subjected to 3D classification, without changing orientation, resulting in two populations of the LBD region. The particles from each LBD class were tracked back to the original, unmodified particle images, which yielded 6 subsets of particles.[66] 3D reconstructions were calculated for each of the six subsets and refined without imposing C4 symmetry. We observed density in the putative ligand- binding pocket in a pattern implying non-stoichiometric binding. Hypothetically, these subsets correspond to six different occupancies of AdA in the InsP$_3$R1 maps: 0-AdA bound, 1 AdA bound, 2 adjacent AdAs bound, 2 opposite AdAs bound, 3 AdAs bound and 4 AdAs bound. However, only the largest class with 3 putative bound AdAs was processed to the highest resolution resulting in the final map of AdA-InsP$_3$R1 at 4.1 Å resolution based on the gold standard FSC 0.143 criteria (Supplementary information, Fig. S2d, e and Table S1). The remaining classes had poorly resolved features in the ligand-binding pocket and did not exhibit sufficient statistics to proceed with further analysis

Image processing and 3D reconstruction of Apo-state in EMAN2. The Apo-InsP$_3$R1 reconstruction began with 155,060 putative particles. Two initial low resolution refinements were performed to eliminate bad particles using the standard multi-resolution quality evaluation in EMAN2 for this purpose, yielding a set of 27,343 particles achieving a better resolution (due to improved self-consistency of the particle set) than the original larger population. This map had an average resolution of 4.5 Å (0.143 criterion following "gold standard" procedures), with significant local variability.[67] This EMAN map and the Apo RELION map were used to produce an initial, incomplete, PDB model. Despite being incomplete, and having mixed quality in different regions, we then took this model, stripped off all sidechains, leaving a simple backbone, then converted this into a density map, which was further subjected to standard phase randomization procedures beyond 7 Å resolution. With these two measures: removing sidechains and phase randomizing, we are confident that any high resolution details emerging in the final model must be produced by the data, not model bias. This initial model was refined using all particles from images less than 2.4 μm underfocus (139,183 particles), which after bad particle elimination left a set of 100,615 particles used in the final refinement. The final map from this process had an overall resolution of 4.3 Å, ranging from 3.5 Å resolution in the TM domain to ~6 Å resolution in the periphery. It is interesting to note that despite going from 27,343 included particles to over 100,000 included particles, the measured resolution changed only very slightly. This demonstrates that our procedures for identifying the particle subsets with the strongest high resolution contribution is reliable (Supplementary information, Fig. S2d and Table S1). In many cases eliminated particles do not disagree with the structure they are being excluded from, but simply reiterate the structure at resolutions where the structure is already well resolved, and may not contribute significantly at higher resolution, due to experimental image quality issues. In such cases eliminating particles will have no real impact on the structure at all. Of greater concern is the possibility that the eliminated particles exhibit an alternative, but equally valid, conformation of the assembly. The key is that we do not claim that the high resolution structures represent the single conformation of the assembly in solution, but simply that this represents one dominate self-consistent population.

We did make numerous attempts to further classify the data to look at structures of states with partial ligand occupancy, etc., but the number of available particles with sufficient high resolution contrast produced only low resolution results. With the level of compositional and conformational variability we believe exists in this system either dramatically improved high resolution contrast or at least an order of magnitude more particles would be required and future studies will aim to obtain such parameters.

Image processing and 3D reconstruction of AdA-InsP$_3$R1 in EMAN2. The full set of 179,730 putative particles was refined using one of the Apo state maps as an initial model. Many of these particles were known to be false positives or have significant image quality issues. Following standard refinement protocols in EMAN2, the Apo-InsP$_3$R1 starting map was independently phase randomized past 10 Å resolution for the even/odd refinements. A standard refinement targeting 5 Å was performed, and the 76,015 particles most self-consistent with this reconstruction was retained for a second refinement targeting 3 Å resolution. Again the most self consistent AdA-InsP$_3$R1 particles were retained (33,680) and a third refinement was done. Since we expect only fractional AdA binding, competitive refinement focused on the TM domain was performed between this AdA-InsP$_3$R1 map and the Apo-InsP$_3$R1 map. This refinement used the 76,015 particle set and produced the population of particles most consistent with AdA-InsP$_3$R1 binding and least consistent with the Apo-state (38,405 particles). Since partial AdA occupancy is also possible within each InsP$_3$R1 tetramer, this population will still not be perfectly homogeneous, but further classification does not improve resolution due to the small number of particles remaining in each population. These particles were then refined to produce the final EMAN2 AdA-InsP$_3$R map, which had an overall resolution of 4.2 Å ranging from 3.6 Å in the TM domain to 8 Å in some peripheral domains.

Model building
A new Apo-InsP$_3$R1 model was constructed directly from the RELION density map using a modified version of our *de novo* modeling protocol. The X-ray structures (PDB IDs: 3UJ4, 3T8S) for the LBD of InsP$_3$R1 were first fit to the density. Starting at the end of the LDB structure and using our previous Apo-InsP$_3$R1 structure (PDB ID: 3JAV) as a roadmap, we rebuilt the Apo-model to be consistent with the higher resolution density features observed. Refinement of the Apo-model was performed using Phenix on the composite Apo-map (default parameters of 'phenix.real_space_refine').[68,69]

To construct the AdA-InsP$_3$R1 model, the new Apo model was first divided into the 10 separate domains and fit to the RELION AdA-InsP$_3$R1 density map. Each domain was then flexibly fit using a combination of FlexEM[70] and Phenix real space refinement with default parameters. Fit-to-density scores and differences between the original model and the flexibly fit model were computed in UCSF Chimera to identify regions (CC < 0.5 and/or > 3 Å RMSD) needing potential further refinement. Once identified, the map and flexibly fit models were imported into Coot and manually refined to optimize both fit to density and model stereochemistry.[71] The newly refined domain models served as anchor points for extending the models. Once the domain models were complete, the individual domains were re-combined into a single model. Iterative automated real space refinement and manual model refinement was then performed with Phenix and Coot. Initial rounds of Phenix refinement enforced "good" secondary structure elements, rotamers and Ramachandran angles; subsequent refinements saw a gradual relaxation of these parameters. A final series of refinements were performed with the complete AdA-InsP$_3$R1 tetramer using the composite AdA-InsP$_3$R1 map (Supplementary information, Fig. S4a). Model statistics, including

Cryo-EM structure of ligand-bound IP3R1 channel
G. Fan et al.

1169

map-model FSCs, fit-to-density, rotamer outliers and ramachandran outliers were monitored during each iteration. The model was considered final once these statistics converged. In both the Apo- and AdA-bound models, full atomistic models were maintained for regions where the majority of sidechain densities were present, including the LBD, ILD, LNK, TM and CTD domains. While some sidechain densities were observed and modeled in the remaining domains, the final model in these domains were rendered only as mainchain atoms. The Apo- InsP$_3$R1 structure was modeled with the following residues: 1–321, 354–532, 536–665, 707–897, 960–1008, 1025–1055, 1042–1102, 1106–1130, 1170–1209, 1224–1317, 1323–1359, 1371–1457, 1473–1490, 1502–1538, 1598–1690, 1786–1879, 1955–2305, 2335–2470, 2519–2739. The AdA- InsP$_3$R1 model consists of residues: 4–321, 353–532, 546–585, 596–665, 707–898, 960–1008, 1024–1055, 1042–1102, 1106–1130, 1170–1209, 1224–1317, 1323–1359, 1371–1457, 1473–1490, 1502–1538, 1598–1690, 1786–1879, 1955–2305, 2335–2470, 2519–2739. The residue numbering is given according to the primary sequence with the GenInfo Identifier (GI) code 17380349, which includes the first methionine.

The ligand densities were visualized by subtracting the structure-factor normalized Apo-map from the final AdA-bound map using 'vop subtract' and contoured to 4σ in UCSF Chimera (Fig. 1c). The location of the densities are consistent with the known InsP$_3$ binding site. Molecular docking computations of AdA with the ligand-bound InsP$_3$R1 model were performed using Autodock Vina[72] followed by evaluation of the docking positions match to the density observed between the β-TF2 and ARM1 domains (Supplementary information, Fig. S6a, b). The final position of AdA gave the highest correlation fit to densities and was a top-scoring binding mode.

Once the models were completed, local map-model FSCs were calculated using EMAN2 (Supplementary information, Fig. S4b). Reported model statistics were generated with Phenix and Molprobity[73] (Supplementary information, Table S1). Map-model visualization and analysis was performed in Coot and UCSF Chimera. Interfaces described were identified with PDBSum[74] and HOLE.[75]

Accession codes

Cryo-EM density maps of InsP$_3$R1 have been deposited in the Electron Microscopy Data Bank (http://www.ebi.ac.uk/pdbe/emdb/) under accession codes EMD-9243, EMD-9244, EMD-9245, EMD-9246, EMDB-9247 and EMD-9248. Corresponding atomic coordinates have been deposited in the Protein Data Bank (http://www.rcsb.org/pdb) under accession codes 6MU1 and 6MU2.

AUTHORS CONTRIBUTIONS

I.I.S. conceived the project; G.F., A.B.S., M.R.B. and I.I.S. purified and characterized the protein; G.F., Z.W. and I.I.S. performed cryo-EM experiments, including cryospecimen preparation and data acquisition; G.F., M.R.B., A.B.S., Z.W. and S.J.L. analysed data; M.L.B. and M.R.B. built the atomic models; M.R.B., M.L.B. and I.I.S. interpreted the models; G.F., M.L.B., M.R.B. and I.I.S. prepared figures and supporting movies; I.I.S. and M.R.B. have written a manuscript with contributions from all authors.

REFERENCES

1. Foskett, J. K., White, C., Cheung, K. H. & Mak, D. O. Inositol trisphosphate receptor Ca^{2+} release channels. *Physiol. Rev.* **87**, 593–658 (2007).
2. Choe, C. U. & Ehrlich, B. E. The inositol 1,4,5-trisphosphate receptor (IP$_3$R) and its regulators: sometimes good and sometimes bad teamwork. *Sci. STKE* **2006**, re15 (2006).
3. Mikoshiba, K. IP$_3$ receptor/Ca^{2+} channel: from discovery to new signaling concepts. *J. Neurochem.* **102**, 1426–1446 (2007).
4. Prole, D. L. & Taylor, C. W. Inositol 1,4,5-trisphosphate receptors and their protein partners as signalling hubs. *J. Physiol.* **11**, 2849–2866 (2016).
5. Fan, G. et al. Gating machinery of InsP$_3$R channels revealed by electron cryomicroscopy. *Nature* **527**, 336–341 (2015).
6. Baker, M. R., Fan, G. & Serysheva, I. I. Structure of IP$_3$R channel: high-resolution insights from cryo-EM. *Curr. Opin. Struct. Biol.* **46**, 38–47 (2017).
7. Taylor, C. W. & Tovey, S. C. IP$_3$ receptors: toward understanding their activation. *Cold Spring Harb. Perspect. Biol.* **2**, a004010, https://doi.org/10.1101/cshperspect.a004010 (2010).
8. Takahashi, M., Tanzawa, K. & Takahashi, S. Adenophostins, newly discovered metabolites of Penicillium brevicompactum, act as potent agonists of the inositol 1,4,5-trisphosphate receptor. *J. Biol. Chem.* **269**, 369–372 (1994).
9. Rossi, A. M., Sureshan, K. M., Riley, A. M., Potter, V. L. & Taylor, C. W. Selective determinants of inositol 1,4,5-trisphosphate and adenophostin A interactions with type 1 inositol 1,4,5-trisphosphate receptors. *Br. J. Pharmacol.* **161**, 1070–1085 (2010).
10. Correa, V. et al. Structural determinants of adenophostin A activity at inositol trisphosphate receptors. *Mol. Pharmacol.* **59**, 1206–1215 (2001).
11. Bezprozvanny, I., Watras, J. & Ehrlich, B. E. Bell-shaped calcium-response curves of Ins(1,4,5)P$_3$- and calcium-gated channels from endoplasmic reticulum of cerebellum. *Nature* **351**, 751–754 (1991).
12. Tu, H., Wang, Z., Nosyreva, E., De Smedt, H. & Bezprozvanny, I. Functional characterization of mammalian inositol 1,4,5-trisphosphate receptor isoforms. *Biophys. J.* **88**, 1046–1055 (2005).
13. Mak, D. O., McBride, S. M., Petrenko, N. B. & Foskett, J. K. Novel regulation of calcium inhibition of the inositol 1,4,5-trisphosphate receptor calcium-release channel. *J. Gen. Physiol.* **122**, 569–581 (2003).
14. Mak, D. O., McBride, S. & Foskett, J. K. ATP-dependent adenophostin activation of inositol 1,4,5-trisphosphate receptor channel gating. Kinetic implications for the durations of calcium puffs in cells. *J. Gen. Physiol.* **117**, 299–314 (2001).
15. Rosenberg, H. J., Riley, A. M., Laude, A. J., Taylor, C. W. & Potter, B. V. Synthesis and Ca^{2+}-mobilizing activity of purine-modified mimics of adenophostin A: a model for the adenophostin-Ins(1,4,5)P$_3$ receptor interaction. *J. Med. Chem.* **46**, 4860–4871 (2003).
16. Rossi, A. M. et al. Synthetic partial agonists reveal key steps in IP$_3$ receptor activation. *Nat. Chem. Biol.* **5**, 631–639 (2009).
17. Saleem, H., Tovey, S. C., Molinski, T. F. & Taylor, C. W. Interactions of antagonists with subtypes of inositol 1,4,5-trisphosphate (IP$_3$) receptor. *Br. J. Pharmacol.* **171**, 3298–3312 (2014).
18. Lin, C. C., Baek, K. & Lu, Z. Apo and InsP-bound crystal structures of the ligand-binding domain of an InsP receptor. *Nat. Struct. Mol. Biol.* **18**, 1172–1174 (2011).
19. Seo, M. D. et al. Structural and functional conservation of key domains in InsP3 and ryanodine receptors. *Nature* **483**, 108–112 (2012).
20. Paknejad, N. & Hite, R. K. Structural basis for the regulation of inositol trisphosphate receptors by Ca^{2+}and IP$_3$. *Nat. Struct. Mol. Biol.* **25**, 660–668 (2018).
21. des Georges, A. et al. Structural basis for gating and activation of RyR1. *Cell* **167**, 145–157 (2016).
22. Bai, X. C., Yan, Z., Wu, J., Li, Z. & Yan, N. The Central domain of RyR1 is the transducer for long-range allosteric gating of channel opening. *Cell Res.* **26**, 995–1006 (2016).
23. Schug, Z. T. et al. Molecular characterization of the inositol 1,4,5-trisphosphate receptor pore-forming segment. *J. Biol. Chem.* **283**, 2939–2948 (2008).
24. Bhanumathy, C., da Fonseca, P. C., Morris, E. P. & Joseph, S. K. Identification of functionally critical residues in the channel domain of inositol trisphosphate receptors. *J. Biol. Chem.* **287**, 43674–43684 (2012).
25. Schug, Z. T. & Joseph, S. K. The role of the S4-S5 linker and C-terminal tail in inositol 1,4,5-trisphosphate receptor function. *J. Biol. Chem.* **281**, 24431–24440 (2006).
26. Long, S. B., Campbell, E. B. & Mackinnon, R. Voltage sensor of Kv1.2: structural basis of electromechanical coupling. *Science* **309**, 903–908 (2005).

1170

27. Doyle, D. A. et al. Crystal structures of a complexed and peptide-free membrane protein- binding domain: molecular basis of peptide recognition by PDZ. *Cell* **85**, 1067–1076 (1996).

28. Fulton, J., Heald, S., Badayl, Y. & Simonson, J. Understanding the effects of concentration on the solvation structure of Ca^{2+} in aqueous solution. I: the perspective on local structure from EXAFS and XANES. *J. Phys. Chem.* **107**, 4688–4696 (2003).

29. Tang, L. et al. Structural basis for Ca^{2+} selectivity of a voltage-gated calcium channel. *Nature* **505**, 56–61 (2014).

30. Mak, D. O. & Foskett, J. K. Single-channel inositol 1,4,5-trisphosphate receptor currents revealed by patch clamp of isolated Xenopus oocyte nuclei. *J. Biol. Chem.* **269**, 29375–29378 (1994).

31. Boehning, D., Joseph, S. K., Mak, D. O. & Foskett, J. K. Single-channel recordings of recombinant inositol trisphosphate receptors in mammalian nuclear envelope. *Biophys. J.* **81**, 117–124 (2001).

32. Ramos-Franco, J., Galvan, D., Mignery, G. A. & Fill, M. Location of the permeation pathway in the recombinant type 1 inositol 1,4,5-trisphosphate receptor. *J. Gen. Physiol.* **114**, 243–250 (1999).

33. Boehning, D., Mak, D. O., Foskett, J. K. & Joseph, S. K. Molecular determinants of ion permeation and selectivity in inositol 1,4,5-trisphosphate receptor Ca^{2+} channels. *J. Biol. Chem.* **276**, 13509–13512 (2001).

34. Yamazaki, H., Chan, J., Ikura, M., Michikawa, T. & Mikoshiba, K. Tyr-167/Trp-168 in type 1/3 inositol 1,4,5-trisphosphate receptor mediates functional coupling between ligand binding and channel opening. *J. Biol. Chem.* **285**, 36081–36091 (2010).

35. Bezprozvanny, I. & Ehrlich, B. E. ATP modulates the function of inositol 1,4,5-trisphosphate-gated channels at two sites. *Neuron* **10**, 1175–1184 (1993).

36. Mak, D. O., McBride, S. & Foskett, J. K. ATP regulation of type 1 inositol 1,4,5-trisphosphate receptor channel gating by allosteric tuning of Ca^{2+} activation. *J. Biol. Chem.* **274**, 22231–22237 (1999).

37. Maes, K. et al. Mapping of the ATP-binding sites on inositol 1,4,5-trisphosphate receptor type 1 and type 3 homotetramers by controlled proteolysis and photoaffinity labeling. *J. Biol. Chem.* **276**, 3492–3497 (2001).

38. Betzenhauser, M. J. et al. ATP modulation of Ca^{2+} release by type-2 and type-3 inositol (1, 4, 5)-triphosphate receptors. Differing ATP sensitivities and molecular determinants of action. *J. Biol. Chem.* **283**, 21579–21587 (2008).

39. Betzenhauser, M. J., Wagner, L. E. 2nd, Park, H. S. & Yule, D. I. ATP regulation of type-1 inositol 1,4,5-trisphosphate receptor activity does not require walker A-type ATP-binding motifs. *J. Biol. Chem.* **284**, 16156–16163 (2009).

40. Mak, D. O. & Foskett, J. K. Inositol 1,4,5-trisphosphate receptors in the endoplasmic reticulum: a single-channel point of view. *Cell Calcium* **58**, 67–78 (2015).

41. Wagner, L. E. 2nd & Yule, D. I. Differential regulation of the InsP3 receptor type-1 and -2 single channel properties by InsP3, Ca^{2+} and ATP. *J. Physiol.* **590**, 3245–3259 (2012).

42. Hamada, K., Miyatake, H., Terauchi, A. & Mikoshiba, K. IP3-mediated gating mechanism of the IP3 receptor revealed by mutagenesis and X-ray crystallography. *Proc. Natl Acad. Sci. USA* **114**, 4661–4666 (2017).

43. Yan, Z. et al. Structure of the rabbit ryanodine receptor RyR1 at near-atomic resolution. *Nature* **517**, 50–55 (2015).

44. Peng, W. et al. Structural basis for the gating mechanism of the type 2 ryanodine receptor RyR2. *Science* **354**, https://doi.org/10.1126/science.aah5324 (2016).

45. Woodier, J., Rainbow, R. D., Stewart, A. J. & Pitt, S. J. Response to Qian and Colvin: zinc-mediated regulation of the cardiac ryanodine receptor occurs via multiple binding sites. *J. Biol. Chem.* **291**, 4267 (2016).

46. Woodier, J., Rainbow, R. D., Stewart, A. J. & Pitt, S. J. Intracellular zinc modulates cardiac ryanodine receptor-mediated calcium release. *J. Biol. Chem.* **290**, 17599–17610 (2015).

47. Du, G. G. & MacLennan, D. H. Functional consequences of mutations of conserved, polar amino acids in transmembrane sequences of the Ca^{2+} release channel (ryanodine receptor) of rabbit skeletal muscle sarcoplasmic reticulum. *J. Biol. Chem.* **273**, 31867–31872 (1998).

48. Miyakawa, T. et al. Ca^{2+}-sensor region of IP3 receptor controls intracellular Ca^{2+} signaling. *EMBO J.* **20**, 1674–1680 (2001).

49. Ionescu, L. et al. Mode switching is the major mechanism of ligand regulation of InsP3 receptor calcium release channels. *J. Gen. Physiol.* **130**, 631–645 (2007).

50. Mak, D. O. & Foskett, J. K. Single-channel kinetics, inactivation, and spatial distribution of inositol trisphosphate IP3 receptors in Xenopus oocyte nucleus. *J. Gen. Physiol.* **109**, 571–587 (1997).

51. Rahman, T. & Taylor, C. W. Dynamic regulation of IP3 receptor clustering and activity by IP3. *Channels (Austin)* **3**, 226–232 (2009).

52. Taufiq, Ur,R., Skupin, A., Falcke, M. & Taylor, C. W. Clustering of InsP3 receptors by InsP3 retunes their regulation by InsP3 and Ca^{2+}. *Nature* **458**, 655–659 (2009).

53. Chakrapani, S. et al. On the structural basis of modal gating behavior in K^+ channels. *Nat. Struct. Mol. Biol.* **18**, 67–74 (2011).

54. Alzayady, K. J. et al. Defining the stoichiometry of inositol 1,4,5-trisphosphate binding required to initiate Ca^{2+} release. *Sci. Signal.* **9**, ra35 (2016).

55. Taylor, C. W. & Konieczny, V. IP3 receptors: take four IP3 to open. *Sci. Signal.* **9**, pe1 (2016).

56. Willegems, K. & Efremov, R. G. Influence of lipid mimetics on gating of ryanodine eceptor. *Structure* **10**, 1303–1313 (2018).

57. Ludtke, S. J. et al. Flexible architecture of InsP3R1 by Cryo-EM. *Structure* **19**, 1192–1199 (2011).

58. Mastronarde, D. N. Automated electron microscope tomography using robust prediction of specimen movements. *J. Struct. Biol.* **152**, 36–51 (2005).

59. Li, X. et al. Electron counting and beam-induced motion correction enable near-atomic-resolution single-particle cryo-EM. *Nat. Methods* **10**, 584–590 (2013).

60. Tang, G. et al. EMAN2: an extensible image processing suite for electron microscopy. *J. Struct. Biol.* **157**, 38–46 (2007).

61. Mindell, J. A. & Grigorieff, N. Accurate determination of local defocus and specimen tilt in electron microscopy. *J. Struct. Biol.* **142**, 334–347 (2003).

62. Scheres, S. H. RELION: Implementation of a Bayesian approach to cryo-EM structure determination. *J. Struct. Biol.* **180**, 519–530 (2012).

63. Henderson, R. et al. Outcome of the first electron microscopy validation task force meeting. *Structure* **20**, 205–214 (2012).

64. Scheres, S. H. & Chen, S. Prevention of overfitting in cryo-EM structure determination. *Nat. Methods* **9**, 853–854 (2012).

65. Kucukelbir, A., Sigworth, F. J. & Tagare, H. D. Quantifying the local resolution of cryo-EM density maps. *Nat. Methods* **11**, 63–65 (2014).

66. Wang, Z. et al. An allosteric transport mechanism for the AcrAB-TolC multidrug efflux pump. *eLife* **6**, e24905 (2017).

67. Bell, J. M., Chen, M., Baldwin, P. R. & Ludtke, S. J. High resolution single particle refinement in EMAN2.1. *Methods* **100**, 25–34 (2016).

68. Adams, P. D. et al. PHENIX: a comprehensive Python-based system for macro-molecular structure solution. *Acta Crystallogr D Biol Crystallogr* 66, (213–221 (2010).

69. DiMaio, F. et al. Improved low-resolution crystallographic refinement with Phenix and Rosetta. *Nat. Methods* **10**, 1102–1104 (2013).

70. Topf, M. et al. Protein structure fitting and refinement guided by cryo-EM density. *Structure* **16**, 295–307 (2008).

71. Emsley, P., Lohkamp, B., Scott, W. G. & Cowtan, K. Features and development of Coot. *Acta Crystallogr. D. Biol. Crystallogr.* **66**, 486–501 (2010).

72. Trott, O. & Olson, A. J. AutoDock Vina: improving the speed and accuracy of docking with a new scoring function, efficient optimization, and multithreading. *J. Comput. Chem.* **31**, 455–461 (2010).

73. Chen, V. B. et al. MolProbity: all-atom structure validation for macromolecular crystallography. *Acta Crystallogr. D. Biol. Crystallogr.* **66**, 12–21 (2010).

74. Laskowski, R. A. et al. PDBsum: a Web-based database of summaries and analyses of all PDB structures. *Trends Biochem. Sci.* **22**, 488–490 (1997).

75. Smart, O. S., Goodfellow, J. M. & Wallace, B. A. The pore dimensions of gramicidin A. *Biophys. J.* **65**, 2455–2460 (1993).